

MorphoSeg: An Uncertainty-Aware Deep Learning Method for Biomedical Segmentation of Complex Cellular Morphologies

Tianhao Zhang^a, Heather J. McCourty^b, Berardo M. Sanchez-Tafolla^b, Anton Nikolaev^b, Lyudmila S. Mihaylova^a

^a*School of Electrical and Electronic Engineering, The University of Sheffield, Sheffield, United Kingdom*

^b*School of Biosciences, The University of Sheffield, Sheffield, United Kingdom*

Abstract

Deep learning has revolutionized medical and biological imaging, particularly in segmentation tasks. However, segmenting biological cells remains challenging due to the high variability and complexity of cell shapes. Addressing this challenge requires high-quality datasets that accurately represent the diverse morphologies found in biological cells. Existing cell segmentation datasets are often limited by their focus on regular and uniform shapes. In this paper, we introduce a novel benchmark dataset of Ntera-2 (NT2) cells, a pluripotent carcinoma cell line, exhibiting diverse morphologies across multiple stages of differentiation, capturing the intricate and heterogeneous cellular structures that complicate segmentation tasks. To address these challenges, we propose an uncertainty-aware deep learning framework for complex cellular morphology segmentation (MorphoSeg) by incorporating sampling of virtual outliers from low-likelihood regions during training. Our comprehensive experimental evaluations against state-of-the-art baselines demonstrate that MorphoSeg significantly enhances segmentation accuracy, achieving up to a 7.74% increase in the Dice Similarity Coefficient (DSC) and a 28.36% reduction in the Hausdorff Distance. These findings highlight the effectiveness of our dataset and methodology in advancing cell segmentation capabilities, especially for complex and variable cell morphologies. The dataset and source code is publicly available at <https://github.com/RanchoGoose/MorphoSeg>.

Keywords: Biomedical Segmentation, Cell Segmentation, Machine Learning, Deep Learning, Ntera-2 Cells, Data Repository, Complex Cell Shapes, Vision Transformer

1. Introduction

The advent of deep learning has significantly advanced the field of medical imaging, particularly in segmentation tasks. While substantial progress has been made in segmenting well-defined objects such as organs in computed tomography (CT) scans [1, 2, 3, 4], cell segmentation presents unique challenges due to the complexity and variability of cell shapes [5, 6, 7, 8]. Existing datasets for cell segmentation [9, 10, 11, 12] often fall short in covering the full spectrum of cell types, hindering the effective training of deep learning models for diverse research applications.

In the broader context of medical image analysis, cell segmentation is crucial yet challenging, particularly due to the high variability in cell stages and the resolutions of medical images. Current state-of-the-art (SOTA) deep learning models, including advanced architectures such as Convolutional Neural Networks (CNNs) [6, 13] and Transformers [1, 3], typically require large, well-annotated datasets, which are resource-intensive to acquire. Beyond focusing on model algorithms, some researchers have shifted towards developing methods for rapid, easy data annotation or advancing weak, semi, or unsupervised learning algorithms to address data insufficiency [14, 15]. However, irregular cell shapes and the need for multi-stage observation remain significant challenges.

In this paper, we present a novel benchmark dataset featuring Ntera-2 cells (NT2) cells [16]. NT2 is a pluripotent carcinoma cell line known for its ability to differentiate into neuro-ectodermal lineages [17]. NT2 cells have previously been shown to transform into neurons, after exposure to all-*trans*-retinoic acid [18]

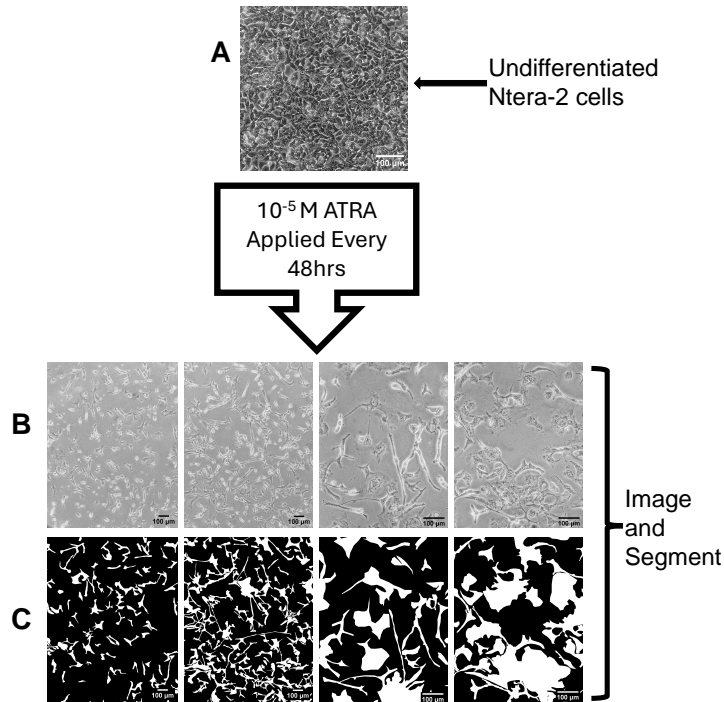


Figure 1. Undifferentiated and Differentiating NT2 Cell Example Images From the Training Set. (A) Undifferentiated Ntera-2 cells. (B) shows the original bright-field images of cells exposed to 10^{-5} M ATRA every 48 hours for 2 weeks. (C) displays the mask created from manual annotations. The images highlight the diverse data set used for training.

(ATRA). During differentiation, NT2 cells exhibit a range of heterogeneous morphologies, as shown in Figure 1, which poses challenges for reliable segmentation. The dataset includes images of NT2 cells at numerous stages of differentiation, spanning from day 7 to day 12, and captures the diverse and complex cell morphologies formed during this period. The complexities can make it difficult to accurately annotate cells, with some cellular features barely discernible even to trained experts. Furthermore, the variability in shape across different stages complicates the segmentation process, necessitating robust deep-learning solutions capable of adapting to such heterogeneity.

To address the aforementioned challenges, we propose a novel unknown-aware enhancement algorithm based on the SOTA medical segmentation framework TransUNet [1]. Our approach involves sampling virtual outliers from the low-likelihood regions of the class-conditional distributions during the training stage to improve the decision boundaries of the segmented objects. This strategy enhances the robustness of the deep learning models, making them effective solutions in such complex scenarios. By incorporating uncertainties into the training objective, our proposed deep learning model achieves strong segmentation of cells with random shapes. When compared against several benchmarks, we demonstrate significant improvements with our proposed dataset: the mean Dice Similarity Coefficient (DSC) increased from 80.35% to 86.57% and the mean Hausdorff Distance (HD95) decreased from 21.98% to 15.75%. These results confirm that our approach not only mitigates data scarcity but also enhances the model’s generalization capabilities across varied cell morphologies. We have provided the full code and pre-trained models with simple inference instructions to facilitate easy implementation and further research by field researchers.

The key contributions of this paper are:

1. Development of a pluripotent carcinoma cell repository, specifically curated to support the development and validation of advanced biological cell segmentation models.
2. Proposal of a practical and scalable framework for cell segmentation that leverages synthetic outliers

and data augmentation to significantly enhance the performance of the SOTA cell segmentation deep-learning models, particularly in scenarios typical of limited data availability.

3. Comprehensive quantitative and qualitative analyses highlighting that the proposed model performs favourably compared to existing techniques.

The remainder of this paper is organized as follows: Section 2 reviews the literature on deep learning methods for biological cell segmentation, and outlier generation methods. Section 3 details our proposed model’s methodology and framework. Section 4 elaborates on the dataset and preprocessing techniques. Section 5 presents experimental setup, results, analyses, and ablation studies, as well as inference and visualization techniques. Finally, Section 6 concludes the paper, summarizing key findings and future research directions.

2. Related Work

2.1. Medical and Biological Image Segmentation.

In recent years, deep learning techniques in computer vision have achieved promising performance in medical image segmentation. Encoder-decoder-based CNN structures have been widely applied, with U-Net and its variants significantly advancing the field [2, 13, 19, 20, 21]. Building upon this structure, UNet++ incorporates densely connected links to enhance the fusion of multi-scale features, improving the analysis of medical images across CT, MRI, and EM modalities [22]. Furthermore, nnU-Net, a self-configuring U-Net, has shown remarkable performance across various segmentation tasks with minimal manual parameter tuning [23, 24]. In terms of segmenting cell structures, the Cellpose model utilizes a two-headed output architecture to predict cell probabilities and spatial organization, effectively handling cells of regular shapes [6]. However, its performance is limited for irregularly shaped cells, as often encountered in advanced disease stages.

Semantic segmentation is pivotal for clinical tasks such as disease detection, differential diagnosis, survival prediction, therapy planning, and treatment response assessment [25, 26, 4, 27, 28, 29]. Besides deep learning methods based on CNN structures, attention mechanisms [30] are extensively employed in semantic segmentation to prioritize salient features. The integration of Vision Transformers (ViTs) [31] into medical segmentation networks has enhanced performance by leveraging self-attention mechanisms [32, 33, 34]. Some research focuses on combining the strengths of transformers with traditional CNN architectures, creating hybrid encoder structures. TransUNet combines CNNs for spatial information extraction with transformers for capturing long-range dependencies, featuring a U-Net structure with self-attention mechanisms to ensure comprehensive image analysis [1]. This integration makes TransUNet particularly effective for detailed medical and biological image segmentation, where preserving spatial hierarchies is crucial. Other research includes employing channel attention to capture boundary-aware features for enhancing polyp segmentation [35]. CellViT replaces the CNN encoder with a transformer block in the U-Net architecture [36]. The recent SAMed model extends the capabilities of the Segment Anything Model (SAM) [37] to medical imaging by employing a Low-rank Adaptation (LoRA) fine-tuning strategy to adapt the large-scale image encoder for medical contexts effectively [3]. This method illustrates the advantage of using extensive pre-trained models for specialized medical segmentation tasks. However, SAM is designed for multi-class segmentation, posing limitations for binary segmentation scenarios.

2.2. Virtual Outliers Synthesis

Outliers in data mining and statistics are typically considered representations of abnormalities, discordants, deviants, or anomalies [38, 39]. In the context of deep learning, outliers are often viewed as anomalies compared to inliers, with multiple deep learning methods developed to detect these outliers [40, 39]. Unlike traditional approaches that focus on outlier detection, recent works in computer vision have explored synthesizing outliers to enhance the accuracy and robustness of deep learning models, particularly in scenarios where datasets are insufficient, such as the medical image classification [39].

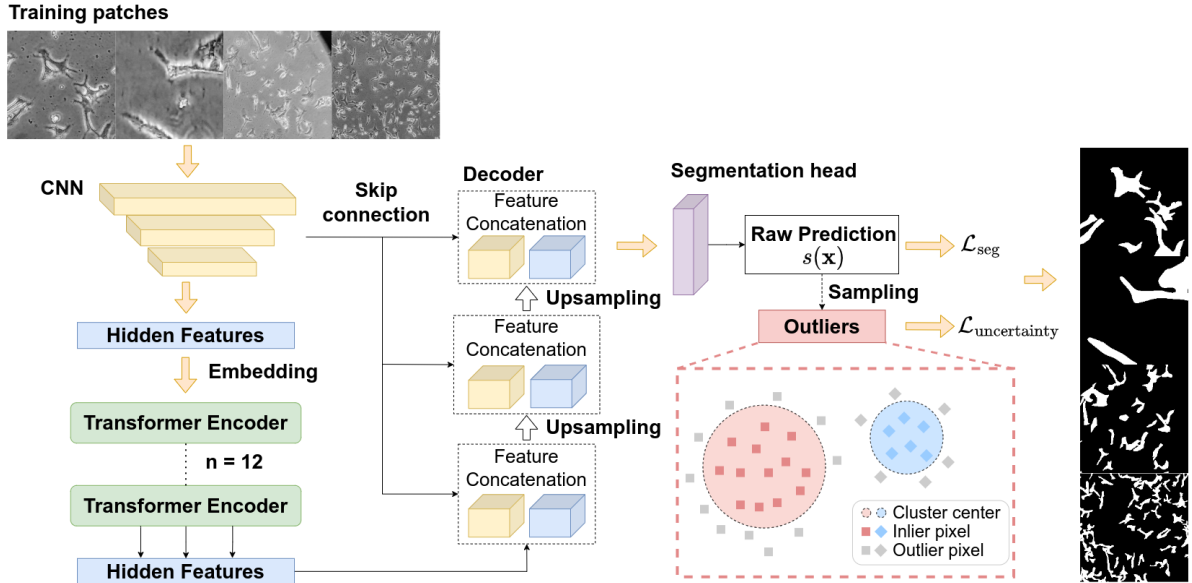


Figure 2. The overall framework of the proposed method, following the architecture of TransUNet [1]. The process for virtual outlier sampling is depicted with red dotted lines. In this framework, we model the feature representations as class-conditional Gaussians and sample virtual outliers v from regions of low likelihood. These virtual outliers contribute to generating the uncertainty loss for regularization. The synthetic segmentation map, incorporating the uncertainty estimation branch $\mathcal{L}_{uncertainty}$, is trained concurrently with the mixed segmentation loss \mathcal{L}_{seg} in Eq. (12).

Further research has leveraged synthetic data to quantify uncertainty, primarily for out-of-distribution (OOD) detection [41, 42, 4]. OOD detection aims to identify conditions unrepresented in the training dataset [43]. In the realm of OOD detection, the challenge is to detect OOD samples; in our case, these include unseen cells in annotations that are difficult for precise human annotation and cells at transitional stages that can be considered OOD. The subtle differences between foreground elements in medical images turn OOD detection into a near-OOD problem, where traditional methods often fall short [44, 45, 46, 47]. In our research, we treat segmentation targets, specifically NT2 cells at various stages, as OOD data. Virtual outlier synthesis has proven effective for OOD detection [41], inspiring us to adapt this approach to enhance the robustness and accuracy of our model for cell segmentation.

Synthesis methods for medical and biological image segmentation remain relatively underexplored. Few synthesis methods have been applied to enhance the training of deep learning models in this area [48, 49, 50]. Our proposed method dynamically estimates class-conditional Gaussian distributions during training, shaping the uncertainty surface over time with our specially formulated loss.

3. Methodology

The overall framework of our approach is depicted in Figure 2. We utilize the TransUNet [1] architecture as the foundational framework for our method. Initially, high-resolution images are subdivided into small patches to align with the input constraints of the vision transformer and enhance the model’s ability to capture cellular details at the pixel level (details in Section 4.2). For the original TransUNet, there are two types of encoders for feature extraction: a hybrid encoder combining a pre-trained CNN and a pure Transformer encoder. We present the hybrid structure in Figure 2 as it provides better results (shown in Section 5.3). It is noteworthy that our method is scalable to different deep learning frameworks since the sampling method works on the raw segmentation predictions (details in Section 3.2). The rest of this section is organized as follows: Section 3.1 provides preliminary information and an overview of the TransUNet framework for image segmentation tasks. In Section 3.2, we present our robust cell segmentation enhancement

via virtual outlier sampling. Section 3.3 introduces the overall uncertainty-aware training objective for MorphoSeg.

3.1. TransUNet for Cell Segmentation

Given an image $\mathbf{x} \in \mathbb{R}^{H \times W \times C}$ with a spatial resolution of $H \times W$ and C channels, our objective is to predict the corresponding pixel-wise label map of the same dimensions. Traditionally, this is achieved by training a CNN (e.g., U-Net) that encodes the image into high-level feature representations and subsequently decodes these representations back to the original spatial resolution. To enhance segmentation accuracy, particularly for cell segmentation, we incorporate a Vision Transformer with self-attention mechanisms for instance segmentation without losing fine-grained information.

Image Sequentialization. For a pure Transformer encoder structure, following [31], we first perform tokenization by reshaping the input \mathbf{x} into a sequence of flattened 2D patches $\{\mathbf{x}_p^i \in \mathbb{R}^{P^2 \cdot C} | i = 1, \dots, N\}$, where each patch is of size $P \times P$ and $N = \frac{HW}{P^2}$ is the number of image patches (*i.e.*, the input sequence length).

Patch Embedding. We map the vectorized patches \mathbf{x}_p into a latent D -dimensional embedding space using a trainable linear projection. To encode the patch spatial information, we learn specific position embeddings which are added to the patch embeddings to retain positional information as follows:

$$\mathbf{z}_0 = [\mathbf{x}_p^1 \mathbf{E}; \mathbf{x}_p^2 \mathbf{E}; \dots; \mathbf{x}_p^N \mathbf{E}] + \mathbf{E}_{pos}, \quad (1)$$

where $\mathbf{E} \in \mathbb{R}^{(P^2 \cdot C) \times D}$ is the patch embedding projection, and $\mathbf{E}_{pos} \in \mathbb{R}^{N \times D}$ denotes the position embedding.

The concatenated sequence \mathbf{T} is processed through the Transformer encoder layers to yield the final representations. Following the the architecture of the vanilla ViT [31], we employ multi-headed self-attention (MSA) [30] (Eq. 3) and multi-layer perceptron (MLP) blocks (Eq. 4). Layer normalization (LN) is applied before each block (Eq. 5), as described in the following equations:

$$\mathbf{Z}_0 = \mathbf{T}, \quad (2)$$

$$\mathbf{Z}'_\ell = \text{MSA}(\text{LN}(\mathbf{Z}_{\ell-1})) + \mathbf{Z}_{\ell-1}, \quad \ell = 1 \dots L, \quad (3)$$

$$\mathbf{Z}_\ell = \text{MLP}(\text{LN}(\mathbf{Z}'_\ell)) + \mathbf{Z}'_\ell, \quad \ell = 1 \dots L, \quad (4)$$

$$\mathbf{Y} = \text{LN}(\mathbf{Z}_L[0]), \quad (5)$$

where L denotes the number of Transformer layers, and $\mathbf{Z}_L[0]$ represents the final layer’s class token representation. The output $\mathbf{Y} \in \mathbb{R}^D$ serves as the input to a classifier head for the task at hand. For segmentation, an effective approach is to upsample the encoded feature representation $\mathbf{z}_L \in \mathbb{R}^{\frac{HW}{P^2} \times D}$ to the full resolution. This involves reshaping the encoded feature from $\frac{HW}{P^2}$ to $\frac{H}{P} \times \frac{W}{P}$, applying a 1×1 convolution to reduce the channel size to the number of classes, and then bilinearly upsampling the feature map to the full resolution $H \times W$ for the final segmentation outcome.

Due to the limited dimensions of ViT input tokens, input image patch sizes $\frac{H}{P} \times \frac{W}{P}$ are often much smaller than the original image resolution $H \times W$ in high-resolution medical images, leading to a loss of low-level details (e.g., cell shape and boundary). TransUNet addresses this by using a CNN-Transformer hybrid model, where a CNN first extracts a feature map from the input. Patch embedding is then applied to 1×1 patches from the CNN feature map instead of raw images, ensuring better retention of details. This method’s efficacy is demonstrated in the comparative analysis of different encoders presented in Table 1 in Section 5.3.

Cascaded Upsampler. Instead of naive upsampling in a ViT, a Cascaded Upsampler (CUP) is implemented, consisting of multiple upsampling steps to decode the hidden features and output the final segmentation mask. After reshaping the sequence of hidden features $\mathbf{z}_L \in \mathbb{R}^{\frac{HW}{P^2} \times D}$ to the shape $\frac{H}{P} \times \frac{W}{P} \times D$, CUP is instantiated by cascading multiple upsampling blocks to reach the full resolution from $\frac{H}{P} \times \frac{W}{P}$ to $H \times W$. Each block consists of a $2 \times$ upsampling operator, a 3×3 convolution layer, and a ReLU layer successively. CUP, together with the hybrid encoder, forms a U-shaped architecture that enables feature aggregation at different resolution levels via skip connections. The upsampling process is also illustrated in Figure 2.

3.2. Robust Cell Segmentation via Virtual Outlier Sampling

To enhance the robustness of our model and accurately simulate the different stages of pluripotent carcinoma cells, we propose the sampling of virtual outliers during the training process. Traditional deep learning models for image segmentation typically utilize CNN frameworks, which compress the latent space into lower dimensions through feature extraction. In contrast, our model is built on a Vision Transformer architecture, which poses challenges in synthesizing virtual outliers directly in the high-dimensional *pixel space* due to its complexity and the optimization difficulties involved. Despite the CNN-Transformer hybrid structure as its encoder in the form of TransUNet, the latent features of high-dimensional images remain in a large matrix. To address this, we opt to sample directly from the output logits of the segmentation map, denoted by $s(\mathbf{x}_i)$, instead of sampling from the latent space.

Given the generic nature of our method, we establish general notations applicable to similar tasks in image classification or segmentation. We model the features of all target classes as conditional multivariate Gaussian distributions:

$$p_\theta(s(\mathbf{x})|y = k) = \mathcal{N}(\boldsymbol{\mu}_k, \boldsymbol{\Sigma}), \quad (6)$$

where $\boldsymbol{\mu}_k$ represents the mean for class $k \in \{1, 2, \dots, K\}$, and $\boldsymbol{\Sigma}$ is the covariance matrix shared across classes. The function $s(\mathbf{x}) \in \mathbb{R}^m$ represents the segmentation map of a cell instance \mathbf{x} , where m is significantly smaller than the input dimension d . In our specific application to the pluripotent carcinoma cell dataset, we focus on two classes: the cells and the background, implying $k = 2$.

To estimate the parameters of the Gaussian distribution, we calculate the empirical class means and covariance matrix from the training samples $\{\mathbf{x}_i, y_i\}_{i=1}^N$:

$$\hat{\boldsymbol{\mu}}_k = \frac{1}{N_k} \sum_{i:y_i=k} s(\mathbf{x}_i), \quad (7)$$

$$\hat{\boldsymbol{\Sigma}} = \frac{1}{N} \sum_{k=1}^K \sum_{i:y_i=k} (s(\mathbf{x}_i) - \hat{\boldsymbol{\mu}}_k) (s(\mathbf{x}_i) - \hat{\boldsymbol{\mu}}_k)^\top. \quad (8)$$

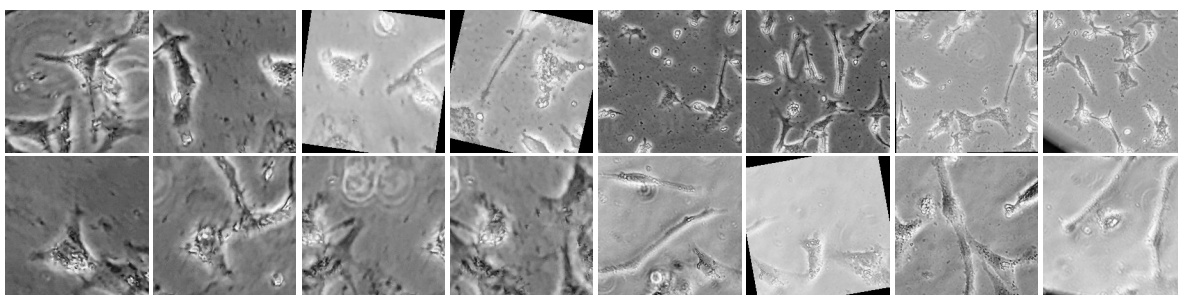
where N_k is the number of objects in class k , and N is the total number of objects. We use online estimation for efficient training, where we maintain a class-conditional queue with $|Q_k|$ object instances from each class. In each iteration, we enqueue the embeddings of objects to their corresponding class-conditional queues and dequeue the same number of object embeddings.

Sampling from the Feature Representation Space We propose sampling virtual outliers from the feature representation space of cell images, utilizing the multivariate distributions estimated from these features. These virtual outliers are designed to refine the decision boundary between different stages of cell development and other outlier data, which may not be adequately represented in the training set.

To accomplish this, we generate virtual outliers \mathcal{V}_k from the ϵ -likelihood region of the estimated class-conditional distribution for each cell stage:

$$\mathcal{V}_k = \left\{ v_k \mid \frac{1}{(2\pi)^{m/2} |\hat{\boldsymbol{\Sigma}}|^{1/2}} \exp \left(-\frac{1}{2} (v_k - \hat{\boldsymbol{\mu}}_k)^\top \hat{\boldsymbol{\Sigma}}^{-1} (v_k - \hat{\boldsymbol{\mu}}_k) \right) < \epsilon \right\}, \quad (9)$$

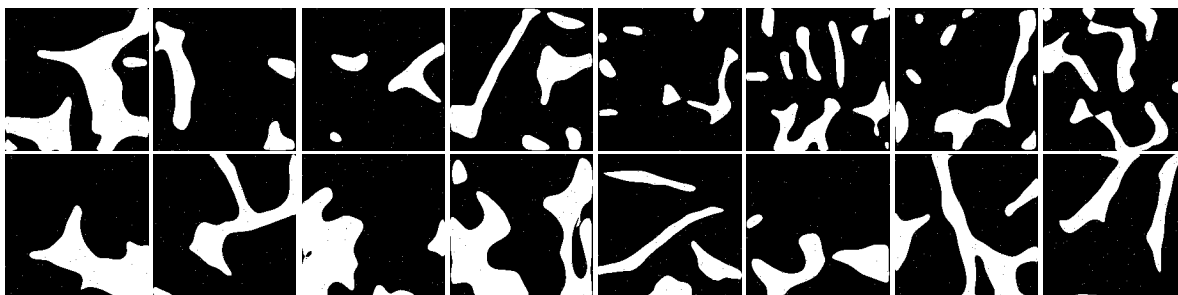
where $v_k \sim \mathcal{N}(\hat{\boldsymbol{\mu}}_k, \hat{\boldsymbol{\Sigma}}_k)$ represents the sampled virtual outliers for class k . These samples are chosen from a sublevel set defined by a small ϵ , ensuring that the outliers are near the decision boundary of the class. We hypothesize that most of the cell pixels are near the boundary of existing cells as shown in Figure 3. Compared to the ground truth masks shown in the second subfigure in Figure 3, the synthesized outliers contain more information about the cells, which are difficult for humans to annotate due to their small size. This strategy aims to enhance the model’s sensitivity to subtle yet critical variations in cell morphology that might indicate different developmental stages or pathological conditions.



(a). Original cell images from the training set



(b). Corresponding ground truth masks



(c). Visualization of the proposed segmentation map with synthesis outliers

Figure 3. Examples showcasing the training with visual outliers. Patches are taken from the training set, presented in sizes of 224×224 and 448×448 . Compared to the ground truth masks, the synthetic outlier samples simulate small cell dots at the pixel level, which are challenging for human annotation. Additionally, small white dots are presented as outliers, which may be difficult to discern without magnification.

3.3. Unknown-aware Training Objective

The objective is to develop an uncertainty-aware deep learning model capable of predicting a segmentation map \hat{S} for input cell images. To this end, we introduce a new training objective for unknown-aware learning, which utilizes virtual outliers as discussed in Section 3.2. We start by defining the standard Dice loss between the predicted pixel scores \hat{y} and the ground truth targets y :

$$\mathcal{L}_{\text{Dice}}(f(\mathbf{x}; \theta), y) = 1 - \frac{2 \sum_i p_i g_i + \epsilon}{\sum_i p_i^2 + \sum_i g_i^2 + \epsilon}, \quad (10)$$

where p_i represents the predicted probabilities for the actual class labels g_i , and ϵ is a small constant introduced to prevent division by zero.

In the case of medical segmentation [51], Dice loss is frequently combined with Cross Entropy loss to form the overall training objective. The Cross Entropy loss is defined as follows:

$$\mathcal{L}_{\text{CE}}(f(\mathbf{x}; \theta), y) = - \sum_i y_i \log(f(\mathbf{x}_i; \theta)), \quad (11)$$

where $f(\mathbf{x}_i; \theta)$ is the model’s output for the input \mathbf{x}_i , and y_i is the corresponding true label.

The overall training objective for medical segmentation, as used in vanilla TransUNet, combines both Cross Entropy and Dice losses [52]. This combined loss function is employed as the primary training loss, defined as:

$$\mathcal{L}_{\text{seg}} = \lambda_1 \mathcal{L}_{\text{CE}}(\hat{S}_l, D(S)) + \lambda_2 \mathcal{L}_{\text{DICE}}(\hat{S}_l, D(S)). \quad (12)$$

The weights λ_1 and λ_2 are used to balance these two terms, typically set to be equally distributed [1].

With the virtual outliers v_k sampled from the predicted segmentation map $s(\mathbf{x}_i)$, we effectively capture the inherent uncertainty of the segmentation process. To make our model uncertainty-aware, we adapt both the Dice loss and Cross Entropy loss for training as follows:

$$\mathcal{L}_{\text{Dice}_{\text{out}}}(f_{\text{syn}}(\mathbf{x}; \theta), y) = 1 - \frac{2 \sum_i p_{\text{syn},i} g_i + \epsilon}{\sum_i p_{\text{syn},i}^2 + \sum_i g_i^2 + \epsilon}, \quad (13)$$

$$\mathcal{L}_{\text{CE}_{\text{out}}}(f_{\text{out}}(\mathbf{x}; \theta), y) = - \sum_i y_i \log(f_{\text{out}}(\mathbf{x}_i; \theta)), \quad (14)$$

where $p_{\text{syn},i}$ represents the predicted probabilities for the actual class labels g_i from the synthetic outputs, and $f_{\text{out}}(\mathbf{x}_i; \theta)$ denotes the model’s output for synthetic data designed to simulate under-represented features.

Furthermore, we model the uncertainty captured by the virtual outliers through a specific loss function:

$$\mathcal{L}_{\text{uncertainty}} = \beta_1 \mathcal{L}_{\text{CE}_{\text{out}}}(\hat{S}_l, D(S)) + \beta_2 \mathcal{L}_{\text{DICE}_{\text{out}}}(\hat{S}_l, D(S)), \quad (15)$$

where β_1 and β_2 are coefficients that weigh the contributions of the cross-entropy and Dice losses, respectively, in quantifying the uncertainty associated with the segmentation of cells.

Overall Training Objective. Although the proposed loss function is initially designed for binary segmentation, it is adaptable for multi-class segmentation scenarios. Our overall training objective integrates the segmentation loss, which includes both Dice and Cross Entropy losses, and a regularization component that addresses model uncertainty:

$$\min_{\theta} \mathbb{E}_{(\mathbf{x}, y) \sim \mathcal{D}} [\lambda \mathcal{L}_{\text{seg}}(\mathbf{x}, y; \theta) + \beta \mathcal{L}_{\text{uncertainty}}(\mathbf{x}, y; \theta)], \quad (16)$$

where λ and β is the weighting coefficient for the uncertainty regularization. The segmentation loss, \mathcal{L}_{seg} , combines the Dice loss, $\mathcal{L}_{\text{DICE}}$, and the cross-entropy loss, \mathcal{L}_{CE} , formulated to effectively handle the segmentation of cells across different stages and morphologies. The uncertainty component, $\mathcal{L}_{\text{uncertainty}}$, leverages synthetic data to enhance the model’s ability to predict underrepresented features and quantify predictive confidence. Ablation studies, detailed in Section 5.4, demonstrate the efficacy of this loss function in improving segmentation accuracy and model robustness.

4. Dataset Analysis

4.1. Data Description

NT2 cells were exposed to 10^{-5} ATRA every 48 hours for 14 days [17, 18]. The cells were imaged using a bright-field microscope on treatment days. ATRA exposure induces neuronal differentiation in NT2 cells, leading to notable morphological changes including an increase in cytoplasm size, elongation of the cell body and neurite extension, as illustrated in Figure 1B.

The NT2 dataset consists of 105 high-resolution raw images of NT2 cells undergoing differentiation, of which 36 images are fully annotated. These images have resolutions primarily around 4000×3000 pixels, enabling detailed morphological analysis and accurate segmentation.

4.2. Data Preprocessing

Data Augmentation. To efficiently train our TransUNet model, we have devised a method to augment the dataset by transforming the high-resolution images into smaller, manageable patches. This is achieved by dividing the images into patches of sizes 224×224 , 448×448 , 1000×1000 , 1500×1500 , and 2000×2000 pixels. We employ an overlapping strategy with an overlap ratio of 0.35 to preserve the spatial context across adjacent patches, which is crucial for capturing the comprehensive spatial information of the cell structures. Combined with the original undivided images and masks, this makes the full dataset for training and testing.

Using this technique, we generate a total of 15,710 patches. These patches are then randomly split into a training set and a testing set, maintaining an 80% to 20% ratio, respectively. This distribution results in 12,568 patches for training and 3,142 patches for testing. To optimize the model’s performance, we implement a data pruning strategy during both the training and testing stages, excluding all patches that do not contain any part of the annotated masks, which will reduce the training set to 10,016 samples for testing.

5. Experiments

5.1. Implementation details

We evaluate our model against established benchmarks including Cellpose and TransUNet, utilizing the AdamW optimizer with exponential learning rate decay on the R50-ViT-B architecture. Specifically for Cellpose, we utilize two of the highest performing pre-trained configurations, cyto3 and cyto2, both set with a cell diameter of 30. These models are trained with a learning rate of 0.01, a weight decay of 5×10^{-5} , and over 200 epochs. The batch size for training is set at 8, with verbose output enabled for detailed progress tracking. During testing, we adapted the Cellpose model to handle larger cells by setting the diameter parameter to 100, with no flow threshold and a cell probability threshold of 0.2, adjusting the channels accordingly to match specific imaging conditions. For the TransUNet, we adhere which includes two types of encoders: a pure Transformer-based encoder, denoted as “ViT-B16,” and a hybrid encoder that combines ResNet-50 with ViT, denoted as “R50-B16”. The input resolution and patch size P are set to 224×224 and 16, respectively. We set the learning rate to 0.01, momentum to 0.9, and weight decay to 1×10^{-4} . The models are trained over 200 epochs, with sampling commencing at the 150th epoch. Both models are trained on two NVIDIA A100 GPUs with a batch size of 256, focusing on 10,000 critical samples by selectively sampling 1,000 pixels per image to enhance training efficiency and effectiveness.

5.2. Evaluation Metrics

To evaluate our method, we considered four key metrics: 1) the average Dice Similarity Coefficient (DSC) [53], 2) the average Hausdorff Distance (HD) [54], 3) the Intersection over Union (IoU) [55], and 4) the mean Average Precision (mAP) [56]. These metrics provide a comprehensive assessment of segmentation accuracy and model performance.

For each class, the unique matching of (y, \hat{y}) splits the predicted and the GT segments into three sets:

- True Positives (TP): the number of correctly predicted pixels that match the ground truth.

- False Positives (FP): the number of pixels incorrectly predicted as part of the object when they are not in the ground truth.
- False negatives (FN): the number of pixels that are missed by the prediction but are present in the ground truth.

The Dice Similarity Coefficient (DSC) is a standard metric for assessing the overlap between the predicted segmentation mask and the ground truth mask. It is defined as:

$$\text{DSC} = \frac{2 \times \text{TP}}{2 \times \text{TP} + \text{FP} + \text{FN}}, \quad (17)$$

where TP, FP, and FN denote the number of true positive, false positive, and false negative pixels, respectively. The Mean DSC is computed by averaging the DSC values across all segmentation instances or classes in the dataset. The Mean DSC provides a robust measure of overall segmentation accuracy, facilitating a comprehensive evaluation of model performance across all classes or instances. Since we only have 1 target class which is the cell, we only use the DSC as the evaluation metric.

To further assess the boundary accuracy, we employ the 95th Percentile Hausdorff Distance (HD95), which offers a more robust measure of the spatial discrepancy between the predicted and ground truth segmentation boundaries. The Hausdorff Distance (HD) between two sets, X and Y , is given by:

$$\text{HD}(X, Y) = \max(h(X, Y), h(Y, X)), \quad (18)$$

where

$$h(X, Y) = \max_{x \in X} \min_{y \in Y} d(x, y), \quad (19)$$

and $d(x, y)$ denotes the Euclidean distance between points $x \in X$ and $y \in Y$.

The HD95 is defined as the 95th percentile of the sorted set of all distances between the predicted and ground truth boundaries:

$$\text{HD95}(X, Y) = \text{Percentile}_{95}(\{d(x, Y) : x \in X\} \cup \{d(y, X) : y \in Y\}), \quad (20)$$

where $d(x, Y) = \min_{y \in Y} d(x, y)$ and $d(y, X) = \min_{x \in X} d(y, x)$. The HD95 metric reduces the influence of outliers by focusing on the 95th percentile distance, providing a robust measure of boundary alignment between the predicted and ground truth segmentations.

The model evaluation should not only use the statistic metrics but also need a qualitative evaluation from the actual segmentation view. The intersection over union (IoU) [57] as an important evaluation index in semantic segmentation measures the overlap of the ground truth and prediction region. It is also calculated:

$$\text{IoU} = \frac{\text{Ground Truth} \cap \text{Prediction}}{\text{Ground Truth} \cup \text{Prediction}}, \quad (21)$$

where \cap denotes the intersection operator and \cup represents the union operator. The IoU is generally calculated based on categories, which is to accumulate the IoU value of each category. The IoU value is to average the sum IoU results of each category to obtain a global evaluation. Therefore, the IoU is actually the mean value, that is, the average crossover ratio (mean IoU).

Finally, the mean Average Precision (mAP) is defined as:

$$\text{mAP} = \frac{1}{N} \sum_{i=1}^N \text{AP}_i, \quad (22)$$

where AP_i represents the average precision for the i -th class, and N is the total number of classes.

These metrics collectively enable a robust evaluation of our model's performance in terms of segmentation accuracy and overall effectiveness.

| Method | | | DSC | HD95 | IoU-0.5 | IoU-0.75 | IoU-0.9 | mAP |
|---------------|---------|---------|--------------|--------------|--------------|--------------|--------------|--------------|
| Framework | Encoder | Loss | ↑ | ↓ | ↑ | ↑ | ↑ | ↑ |
| Cellpose [6] | cyto3 | | 63.66 | 137.9 | 25.31 | 12.35 | 3.641 | 48.51 |
| | cyto2 | | 48.15 | 181.5 | 19.02 | 8.220 | 2.569 | 36.78 |
| TransUNet [1] | ViT-B16 | | 72.47 | 38.21 | 76.42 | 30.19 | 3.019 | 36.54 |
| | R50-B16 | | 80.35 | 21.98 | 88.00 | 58.67 | 9.220 | 51.97 |
| MorphoSeg | ViT-B16 | Balance | 72.78 | 38.69 | 77.35 | 30.19 | 3.787 | 37.46 |
| | | Norm | 74.24 | 36.82 | 81.54 | 43.82 | 4.765 | 38.96 |
| | | Pareto | 73.67 | 37.10 | 80.43 | 42.66 | 3.433 | 37.58 |
| | R50-B16 | Balance | 86.33 | 16.33 | 93.02 | 79.68 | 20.11 | 64.27 |
| | | Norm | 84.40 | 26.37 | 91.64 | 72.50 | 11.30 | 58.48 |
| | | Pareto | 86.57 | 15.75 | 93.02 | 80.01 | 21.87 | 64.96 |

Table 1. Comparison on our proposed cell dataset. All methods incorporating Outlier Synthesis are trained with a sample size of 100,000, and the selection count is set to 10,000. ↑ indicates that larger values are preferable, while ↓ indicates that smaller values are better. All numerical values are presented as percentages. **Bold** numbers indicate superior results.

5.3. Comparison with Baselines

Table 1 presents the main results of the proposed approach, which includes training with outliers compared to the Cellpose pretrained on cyto3 and cyto2, and TransUNet of ViT-B16 and R50-B16 variants. Despite the advantages of the Cellpose model, such as requiring a smaller number of annotations, it does not offer superior performance due to its reliance on the flow and diameter of cells. In our study, these characteristic properties vary across different stages, and the irregular shapes of cells do not provide consistent diameters for effective segmentation. In comparison, our training approach with Outlier Synthesis enhances the performance significantly over the state-of-the-art TransUNet across all types of loss combinations.

5.4. Ablation Studies

Incorporating Uncertainty into Loss Function Design. To determine the optimal values for the weight parameters λ and β in Equation.(16), we evaluate three sophisticated approaches to weight the loss components, tailored for enhanced model training and testing. The **Original Balancing** method, consistent with TranUNet, evenly distributes weights across all loss components, simplifying optimization but potentially overlooking specific task requirements within the model. Alternatively, the **Normalized Losses** method dynamically scales each loss component by its magnitude:

$$\mathcal{L}_{\text{norm}} = \sum_i \frac{\mathcal{L}_i}{\|\mathcal{L}_i\|} + \epsilon, \quad (23)$$

where \mathcal{L}_i denotes individual loss components, $\|\cdot\|$ signifies the norm operation applied to each loss component to normalize its scale, and ϵ is a small constant to prevent division by zero. This adjustment ensures that hyperparameters λ_i are iteratively tuned to maintain balance among the loss components. A refinement of this approach normalizes subsequent losses relative to the first, calculated as:

$$\mathcal{L}_{\text{pareto}} = \mathcal{L}_{\text{loss}} + \sum_{i \neq \text{loss}} \frac{\mathcal{L}_i}{\|\mathcal{L}_i / \mathcal{L}_{\text{loss}}\|}, \quad (24)$$

which potentially provides a more rational scaling by relating all losses back to the primary loss component. Lastly, the **Pareto Optimization** strategy [58], aims to achieve a Pareto efficient solution by treating each loss as an objective in a multi-objective optimization framework, wherein improvements in one objective are sought without significant compromises in others, facilitating an equilibrium that optimizes overall model performance.

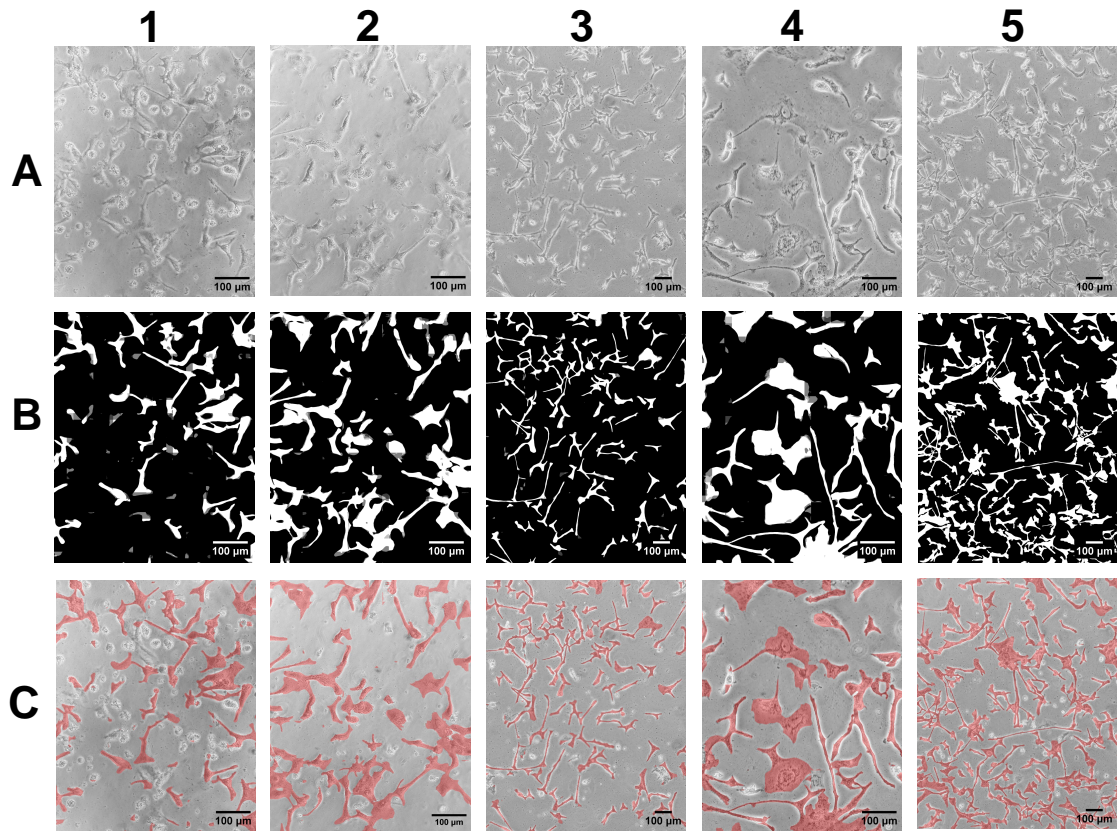


Figure 4. Visualization of Ntera-2 Cell Segmentation in the Testing Dataset: Original Images, Segmentation Masks, and Overlays. Row A displays the original images, Row B displays the segmentation mask and Row C displays the mask overlay on the original image. Image set 1 highlights the ability of the network to segment cells in an unfocused image. Image set 2 highlights the ability of the network to segment cells despite low contrast and unclear cell borders. Images 3 and 4 display ability of the network to segment high-quality images at different magnifications, $\times 10$ and $\times 25$, respectively.

5.5. Patch-Based Approach for High-Resolution Inference and Visualization

Given the inherent limitations of Vision Transformers, where token size constraints can result in vague and imprecise inference on large images, we propose an advanced patch-based inference technique to address the sensitivity to pixel-level cellular details. This approach enhances segmentation accuracy for high-resolution biological cell images while making the framework more practical and accessible for researchers. Example visualizations of the results are presented in Figure 4.

During a single image inference stage, the image is initially subdivided into patches of size 224×224 , similar to the data augmentation strategy presented in Section 4.2. This subdivision allows the model to focus on and accurately detect fine-grained variations at the boundaries of the Ntera-2 cells and their surrounding environment. Each patch undergoes a separate inference process. To preserve the global spatial context, we incorporate an overlapping strategy with a 56-pixel margin. This overlap ensures continuity and minimizes edge artifacts. The inference results from the patches are then combined using an average pooling strategy and visualized as segmentation masks, shown in red in Figure 4. This end-to-end training and visualization strategy significantly facilitates the application of our framework, enabling researchers to use it without requiring further modifications.

6. Conclusion and Future Work

In this paper, we introduced a novel data repository containing differentiating NT2 cells, designed to facilitate the segmentation of complex cell morphologies. This dataset requires pixel-level segmentation, which presents new challenges for accurately segmenting cells with intricate shapes. To address these challenges, we proposed an uncertainty-aware segmentation method MorphoSeg enhancing the base TranUNet by training on virtual outliers sampled near the feature representation space, thereby increasing the model’s sensitivity to small pixel variations and morphological changes across different cell stages. This enhancement makes our MorphoSeg more robust and effective for segmenting complex and irregularly shaped cells.

The experimental results demonstrate that the proposed MorphoSeg outperforms existing benchmarks, including Cellpose and TransUNet. Our best-performing model, MorphoSeg with a hybrid encoder, showed a notable improvement in performance metrics, achieving a 6.23% increase in the Dice Similarity Coefficient (DSC). This statistic measures the similarity between the segmented cells and the ground truth. A reduction in HD95 (Hausdorff Distance at the 95th percentile) was also measured, indicating a decreased spatial discrepancy between the predicted and actual segmentation boundaries compared to the baseline configuration.

By providing comprehensive visualizations and complete code, we aim to contribute to not only advance further research in this emerging domain but also to serve as a practical solution for cell segmentation and visualization in diverse medical AI applications.

Future Work: Building on the proposed NT2 cells dataset, future research will address the challenge of segmenting complex cell morphologies, particularly those with substantial overlapping regions, which remain a significant obstacle to achieving accurate segmentation. Further efforts will focus on developing advanced deep-learning methods for biological AI to overcome these challenges.

Acknowledgments

We express our gratitude to the UK Engineering and Physical Sciences Research Council (EPSRC) for their support through the following projects: EP/V026747/1 (Trustworthy Autonomous Systems Node in Resilience) and EP/T013265/1 (NSF-EPSRC: ShiRAS. Towards Safe and Reliable Autonomy in Sensor Driven Systems). We also acknowledge the support of the National Science Foundation (NSF) under Grant No. ECCS 1903466 for the ShiRAS project. For the purpose of open access, the authors have applied a Creative Commons Attribution (CC BY) licence to any Author Accepted Manuscript (AAM) version arising from this work.

References

- [1] J. Chen, Y. Lu, Q. Yu, X. Luo, E. Adeli, Y. Wang, L. Lu, A. L. Yuille, Y. Zhou, Transunet: Transformers make strong encoders for medical image segmentation, arXiv preprint arXiv:2102.04306 (2021). [1](#), [2](#), [3](#), [4](#), [8](#), [11](#)
- [2] O. Ronneberger, P. Fischer, T. Brox, U-net: Convolutional networks for biomedical image segmentation, in: International Conference on Medical image computing and computer-assisted intervention, Springer, 2015, pp. 234–241. [1](#), [3](#)
- [3] K. Zhang, D. Liu, Customized segment anything model for medical image segmentation, arXiv preprint arXiv:2304.13785 (2023). [1](#), [3](#)
- [4] T. Zhao, K. Cao, J. Yao, I. Noguez, L. Lu, L. Huang, J. Xiao, Z. Yin, L. Zhang, 3D graph anatomy geometry-integrated network for pancreatic mass segmentation, diagnosis, and quantitative patient management, in: Proceedings of the IEEE/CVF Conference on Computer Vision and Pattern Recognition, 2021, pp. 13743–13752. [1](#), [3](#), [4](#)
- [5] M. Saha, C. Chakraborty, Her2net: A deep framework for semantic segmentation and classification of cell membranes and nuclei in breast cancer evaluation, IEEE Transactions on Image Processing 27 (5) (2018) 2189–2200. [1](#)
- [6] C. Stringer, T. Wang, M. Michaelos, M. Pachitariu, Cellpose: a generalist algorithm for cellular segmentation, Nature methods 18 (1) (2021) 100–106. [1](#), [3](#), [11](#)
- [7] V. Petukhov, R. J. Xu, R. A. Soldatov, P. Cadinu, K. Khodosevich, J. R. Moffitt, P. V. Kharchenko, Cell segmentation in imaging-based spatial transcriptomics 40 (2021) 345–354. [1](#)
- [8] C. Edlund, T. R. Jackson, N. Khalid, N. Bevan, T. Dale, A. Dengel, S. Ahmed, J. Trygg, R. Sjögren, Livecell—a large-scale dataset for label-free live cell segmentation 18 (2021) 1038–1045. [1](#)
- [9] U. Israel, M. Marks, R. Dilip, Q. Li, M. Schwartz, E. Pradhan, E. Pao, S. Li, A. Pearson-Goulart, P. Perona, et al., A foundation model for cell segmentation, bioRxiv [doi:10.1101/2023.11.17.567630](https://doi.org/10.1101/2023.11.17.567630). [1](#)
- [10] C. Edlund, T. R. Jackson, N. Khalid, N. Bevan, T. Dale, A. Dengel, S. Ahmed, J. Trygg, R. Sjögren, Livecell—a large-scale dataset for label-free live cell segmentation, Nature methods 18 (9) (2021) 1038–1045. [1](#)

- [11] D. A. Van Valen, T. Kudo, K. M. Lane, D. N. Macklin, N. T. Quach, M. M. DeFelice, I. Maayan, Y. Tanouchi, E. A. Ashley, M. W. Covert, [Deep learning automates the quantitative analysis of individual cells in live-cell imaging experiments](#), *PLOS Computational Biology* 12 (11) (2016) 1–24. doi:10.1371/journal.pcbi.1005177. URL <https://doi.org/10.1371/journal.pcbi.1005177> 1
- [12] E. Moen, E. Borba, G. Miller, M. Schwartz, D. Bannon, N. Koe, I. Camplisson, D. Kyme, C. Pavelchek, T. Price, T. Kudo, E. Pao, W. Graf, D. Van Valen, [Accurate cell tracking and lineage construction in live-cell imaging experiments with deep learning](#), bioRxiv (2019). arXiv:<https://www.biorxiv.org/content/early/2019/10/14/803205.full.pdf>, doi:10.1101/803205. URL <https://www.biorxiv.org/content/early/2019/10/14/803205> 1
- [13] X. Li, H. Chen, X. Qi, Q. Dou, C.-W. Fu, P. A. Heng, H-DenseUNet: Hybrid densely connected UNet for liver and liver tumor segmentation from CT volumes, *IEEE Transactions on Medical Imaging* (2017). 1, 3
- [14] T. Zhao, Z. Yin, Weakly supervised cell segmentation by point annotation 40 (2021) 2736–2747. 1
- [15] M. C. Robitaille, J. M. Byers, J. A. Christodoulides, M. P. Raphael, Self-supervised machine learning for live cell imagery segmentation 5 (2022) 1162–8. 1
- [16] H. J. McCourty, T. Zhang, A. Nikolaev, B. M. Sanchez-Tafoll, L. S. Mihaylova, Dataset of Ntera-2 cells for segmentation (2024). doi:<https://doi.org/10.15131/shef.data.25604421>. 1
- [17] S. Pleasure, V. Lee, Ntera 2 cells: A human cell line which displays characteristics expected of a human committed neuronal progenitor cell, *Journal of Neuroscience Research* 34 (1993) 585–602. 1, 9
- [18] P. W. Andrews, Retinoic acid induces neuronal differentiation of a cloned human embryonal carcinoma cell line in vitro, *Developmental Biology* 103 (2) (1984) 285–293. 1, 9
- [19] S. Liu, D. Xu, S. K. Zhou, O. Pauly, S. Grbic, T. Mertelmeier, J. Wicklein, A. Jerebko, W. Cai, D. Comaniciu, 3d anisotropic hybrid network: Transferring convolutional features from 2d images to 3d anisotropic volumes, in: *International Conference on Medical Image Computing and Computer-Assisted Intervention*, Springer, 2018, pp. 851–858. 3
- [20] F. Milletari, N. Navab, S.-A. Ahmadi, V-net: Fully convolutional neural networks for volumetric medical image segmentation, in: *2016 Fourth International Conference on 3D Vision (3DV)*, IEEE, 2016, pp. 565–571. 3
- [21] L. Yu, X. Yang, H. Chen, J. Qin, P. Heng, Volumetric convnets with mixed residual connections for automated prostate segmentation from 3D MR images, in: *AAAI*, 2017. 3
- [22] Z. Zhou, M. M. R. Siddiquee, N. Tajbakhsh, J. Liang, Unet++: Redesigning skip connections to exploit multiscale features in image segmentation, *IEEE Transactions on Medical Imaging* 39 (6) (2019) 1856–1867. 3
- [23] F. Isensee, J. Petersen, A. Klein, D. Zimmerer, P. F. Jaeger, S. Kohl, J. Wasserthal, G. Koehler, T. Norajitra, S. Wirkert, et al., nnu-net: Self-adapting framework for u-net-based medical image segmentation, arXiv preprint arXiv:1809.10486 (2018). 3
- [24] F. Isensee, P. F. Jaeger, S. A. Kohl, J. Petersen, K. H. Maier-Hein, nnu-net: a self-configuring method for deep learning-based biomedical image segmentation, *Nature methods* 18 (2) (2021) 203–211. 3
- [25] L. C. Chu, S. Park, S. Kawamoto, Y. Wang, Y. Zhou, W. Shen, Z. Zhu, Y. Xia, L. Xie, F. Liu, et al., Application of deep learning to pancreatic cancer detection: lessons learned from our initial experience, *Journal of the American College of Radiology* 16 (9) (2019) 1338–1342. 3
- [26] J. De Fauw, J. R. Ledsam, B. Romera-Paredes, S. Nikolov, N. Tomasev, S. Blackwell, H. Askham, X. Glorot, B. O’Donoghue, D. Visentin, et al., Clinically applicable deep learning for diagnosis and referral in retinal disease, *Nature Medicine* 24 (9) (2018) 1342–1350. 3
- [27] J. Yao, K. Cao, Y. Hou, J. Zhou, Y. Xia, I. Noguez, Q. Song, H. Jiang, X. Ye, J. Lu, et al., Deep learning for fully automated prediction of overall survival in patients undergoing resection for pancreatic cancer: A retrospective multicenter study., *Annals of Surgery* (2022). 3
- [28] H. Tang, X. Chen, Y. Liu, Z. Lu, J. You, M. Yang, S. Yao, G. Zhao, Y. Xu, T. Chen, et al., Clinically applicable deep learning framework for organs at risk delineation in ct images, *Nature Machine Intelligence* 1 (10) (2019) 480–491. 3
- [29] P. Kickingreder, F. Isensee, I. Tursunova, J. Petersen, U. Neuberger, D. Bonekamp, G. Brugnara, M. Schell, T. Kessler, M. Foltyn, et al., Automated quantitative tumour response assessment of MRI in neuro-oncology with artificial neural networks: a multicentre, retrospective study, *The Lancet Oncology* 20 (5) (2019) 728–740. 3
- [30] A. Vaswani, N. Shazeer, N. Parmar, J. Uszkoreit, L. Jones, A. N. Gomez, L. Kaiser, I. Polosukhin, Attention is all you need, *Advances in Neural Information Processing Systems* 30 (2017). 3, 5
- [31] A. Dosovitskiy, L. Beyer, A. Kolesnikov, D. Weissenborn, X. Zhai, T. Unterthiner, M. Dehghani, M. Minderer, G. Heigold, S. Gelly, et al., An image is worth 16x16 words: Transformers for image recognition at scale, *ICLR* (2021). 3, 5
- [32] A. Hatamizadeh, Y. Tang, V. Nath, D. Yang, A. Myronenko, B. Landman, H. R. Roth, D. Xu, Unetr: Transformers for 3d medical image segmentation, in: *Proceedings of the IEEE/CVF Winter Conference on Applications of Computer Vision*, 2022, pp. 574–584. 3
- [33] A. Hatamizadeh, V. Nath, Y. Tang, D. Yang, H. R. Roth, D. Xu, Swin unetr: Swin transformers for semantic segmentation of brain tumors in mri images, in: *International MICCAI Brainlesion Workshop*, Springer, 2022, pp. 272–284. 3
- [34] Y. Tang, D. Yang, W. Li, H. R. Roth, B. Landman, D. Xu, V. Nath, A. Hatamizadeh, Self-supervised pre-training of swin transformers for 3d medical image analysis, in: *Proceedings of the IEEE/CVF Conference on Computer Vision and Pattern Recognition*, 2022, pp. 20730–20740. 3
- [35] T. Zhou, Y. Zhou, K. He, C. Gong, J. Yang, H. Fu, D. Shen, Cross-level feature aggregation network for polyp segmentation, *Pattern Recognition* 140 (2023) 109555. 3
- [36] F. Hörst, M. Rempe, L. Heine, C. Seibold, J. Keyl, G. Baldini, S. Ugurel, J. Siveke, B. Grünwald, J. Egger, J. Kleesiek, [Cellvit: Vision transformers for precise cell segmentation and classification](#), *Medical Image Analysis* 94 (2024) 103143. doi:<https://doi.org/10.1016/j.media.2024.103143>.

- URL <https://www.sciencedirect.com/science/article/pii/S1361841524000689> 3
- [37] A. Kirillov, E. Mintun, N. Ravi, H. Mao, C. Rolland, L. Gustafson, T. Xiao, S. Whitehead, A. C. Berg, W.-Y. Lo, et al., Segment anything, arXiv preprint arXiv:2304.02643 (2023). 3
- [38] C. C. Aggarwal, *An Introduction to Outlier Analysis*, Springer International Publishing, Cham, 2017, pp. 1–34. doi: 10.1007/978-3-319-47578-3_1. URL https://doi.org/10.1007/978-3-319-47578-3_1 3
- [39] A. Boukerche, L. Zheng, O. Alfandi, Outlier detection: Methods, models, and classification, ACM Computing Surveys (CSUR) 53 (3) (2020) 1–37. 3
- [40] H. Wang, M. J. Bah, M. Hammad, Progress in outlier detection techniques: A survey, Ieee Access 7 (2019) 107964–108000. 3
- [41] X. Du, Z. Wang, M. Cai, Y. Li, Vos: Learning what you don’t know by virtual outlier synthesis, in: Proceedings of the International Conference on Learning Representations, 2022. 4
- [42] R. He, Z. Han, X. Lu, Y. Yin, Ronf: Reliable outlier synthesis under noisy feature space for out-of-distribution detection (2022) 4242–4251. 4
- [43] M. Yuan, Y. Xia, H. Dong, Z. Chen, J. Yao, M. Qiu, K. Yan, X. Yin, Y. Shi, X. Chen, Z. Liu, B. Dong, J. Zhou, L. Lu, L. Zhang, L. Zhang, Devil is in the queries: Advancing mask transformers for real-world medical image segmentation and out-of-distribution localization, in: Proceedings of the IEEE/CVF Conference on Computer Vision and Pattern Recognition (CVPR), 2023, pp. 23879–23889. 4
- [44] J. Winkens, R. Bunel, A. G. Roy, R. Stanforth, V. Natarajan, J. R. Ledsam, P. MacWilliams, P. Kohli, A. Karthikesalingam, S. Kohl, et al., Contrastive training for improved out-of-distribution detection, arXiv preprint arXiv:2007.05566 (2020). 4
- [45] J. Ren, S. Fort, J. Liu, A. G. Roy, S. Padhy, B. Lakshminarayanan, A simple fix to mahalanobis distance for improving near-ood detection, arXiv preprint arXiv:2106.09022 (2021). 4
- [46] H. Mirzaei, M. Salehi, S. Shahabi, E. Gavves, C. G. Snoek, M. Sabokrou, M. H. Rohban, Fake it till you make it: Near-distribution novelty detection by score-based generative models, arXiv preprint arXiv:2205.14297 (2022). 4
- [47] X. Dong, J. Guo, A. Li, W.-T. Ting, C. Liu, H. Kung, Neural mean discrepancy for efficient out-of-distribution detection, in: Proceedings of the IEEE/CVF Conference on Computer Vision and Pattern Recognition, 2022, pp. 19217–19227. 4
- [48] C. Bowles, C. Qin, R. Guerrero, R. Gunn, A. Hammers, D. A. Dickie, M. Valdés Hernández, J. Wardlaw, D. Rueckert, Brain lesion segmentation through image synthesis and outlier detection, NeuroImage: Clinical 16 (2017) 643–658. doi:<https://doi.org/10.1016/j.nicl.2017.09.003>. URL <https://www.sciencedirect.com/science/article/pii/S2213158217302164> 4
- [49] V. Thambawita, P. Salehi, S. A. Sheshkal, S. A. Hicks, H. L. Hammer, S. Parasa, T. d. Lange, P. Halvorsen, M. A. Riegler, Singan-seg: Synthetic training data generation for medical image segmentation, PloS one 17 (5) (2022) e0267976. 4
- [50] D. Nie, D. Shen, Adversarial confidence learning for medical image segmentation and synthesis, International Journal of Computer Vision 128 (10) (2020) 2494–2513. doi:10.1007/s11263-020-01321-2. URL <https://doi.org/10.1007/s11263-020-01321-2> 4
- [51] T.-Y. Lin, P. Goyal, R. Girshick, K. He, P. Dollar, Focal loss for dense object detection, Vol. 42 of 2, 2017, pp. 2999–3007. 8
- [52] Y. Tian, M. Shi, Y. Luo, A. Kouhana, T. Elze, M. Wang, Fairseg: A large-scale medical image segmentation dataset for fairness learning using segment anything model with fair error-bound scaling, in: International Conference on Learning Representations (ICLR), 2024. 8
- [53] R. R. Shamir, Y. Duchin, J. Kim, G. Sapiro, N. Harel, Continuous dice coefficient: a method for evaluating probabilistic segmentations, arXiv preprint arXiv:1906.11031 (2019). 9
- [54] D. P. Huttenlocher, G. A. Klanderman, W. J. Rucklidge, Comparing images using the hausdorff distance, IEEE Transactions on pattern analysis and machine intelligence 15 (9) (1993) 850–863. 9
- [55] H. Rezatofighi, N. Tsoi, J. Gwak, A. Sadeghian, I. Reid, S. Savarese, Generalized intersection over union: A metric and a loss for bounding box regression, in: Proceedings of the IEEE/CVF conference on computer vision and pattern recognition, 2019, pp. 658–666. 9
- [56] P. Henderson, V. Ferrari, End-to-end training of object class detectors for mean average precision, in: Computer Vision–ACCV 2016: 13th Asian Conference on Computer Vision, Taipei, Taiwan, November 20–24, 2016, Revised Selected Papers, Part V 13, Springer, 2017, pp. 198–213. 9
- [57] M. A. Rahman, Y. Wang, Optimizing intersection-over-union in deep neural networks for image segmentation, in: Proceedings of the International Symposium on Visual Computing, Springer, 2016, pp. 234–244. 10
- [58] O. Sener, V. Koltun, Multi-task learning as multi-objective optimization, in: S. Bengio, H. Wallach, H. Larochelle, K. Grauman, N. Cesa-Bianchi, R. Garnett (Eds.), Advances in Neural Information Processing Systems 31, Curran Associates, Inc., 2018, pp. 525–536. 11